https://doi.org/10.1007/s11467-022-1241-7

RESEARCH ARTICLE

Ultrasensitive solar-blind ultraviolet detection and optoelectronic neuromorphic computing using α-In_2Se_3 phototransistors

Yuchen Cai[1,2,*], Jia Yang[1,2,*], Feng Wang[1,2,†], Shuhui Li[1,2], Yanrong Wang[1,2], Xueying Zhan[1,2],
Fengmei Wang[1,2], Ruiqing Cheng[3,‡], Zhenxing Wang[1,2,§], Jun He[3]

[1] CAS Key Laboratory of Nanosystem and Hierarchical Fabrication, National Center for Nanoscience and Technology, Beijing 100190, China
[2] Center of Materials Science and Optoelectronics Engineering, University of Chinese Academy of Sciences, Beijing 100049, China
[3] Key Laboratory of Artificial Micro- and Nano-structures of Ministry of Education, School of Physics and Technology, Wuhan University, Wuhan 430072, China
Corresponding authors. E-mail: [†]wangf@nanoctr.cn, [‡]chengrq@whu.edu.cn, [§]wangzx@nanoctr.cn
[*]These authors contributed equally.
Received October 17, 2022; accepted December 5, 2022

Supporting Information

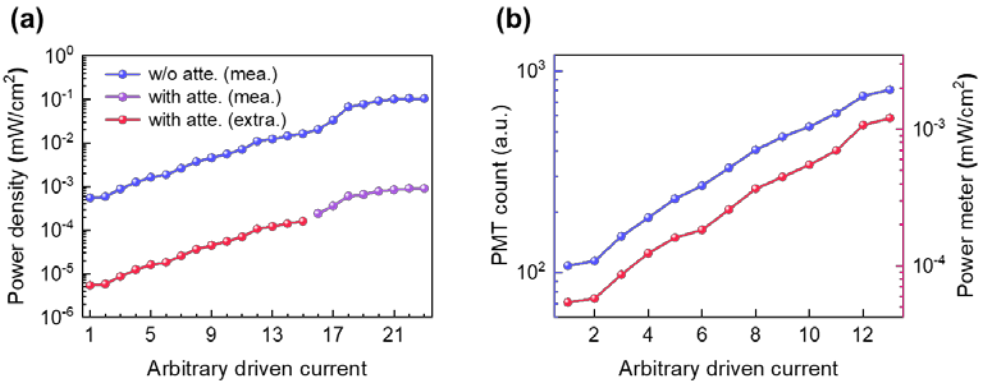

Supplementary Fig. S1 Calibration of the 275 nm light sources. **(a)** Measured (blue and purple) and extrapolated (red) power density using a power meter. The line in blue was measured without an attenuator. **(b)** Comparison between measured PMT count (blue) and extrapolated power density (red).

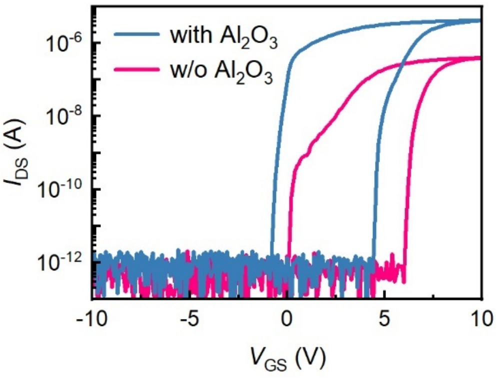

Supplementary Fig. S2 Transfer curves of the devices with and without the top Al_2O_3 layer. V_{DS}: 1 V.

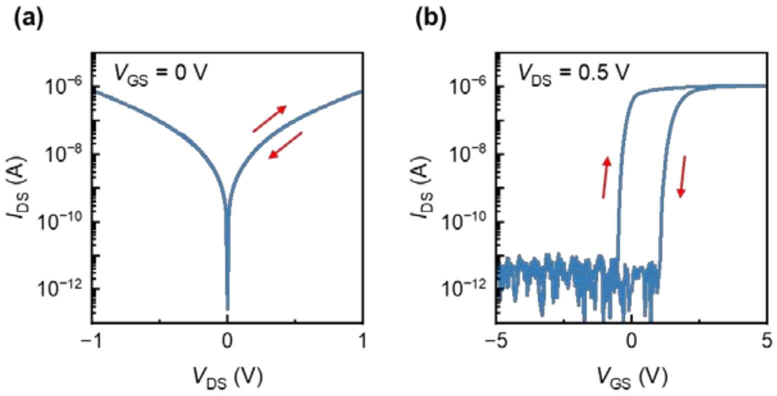

Supplementary Fig. S3 **(a)** Output and **(b)** transfer curves of the α-In_2Se_3 phototransistor.

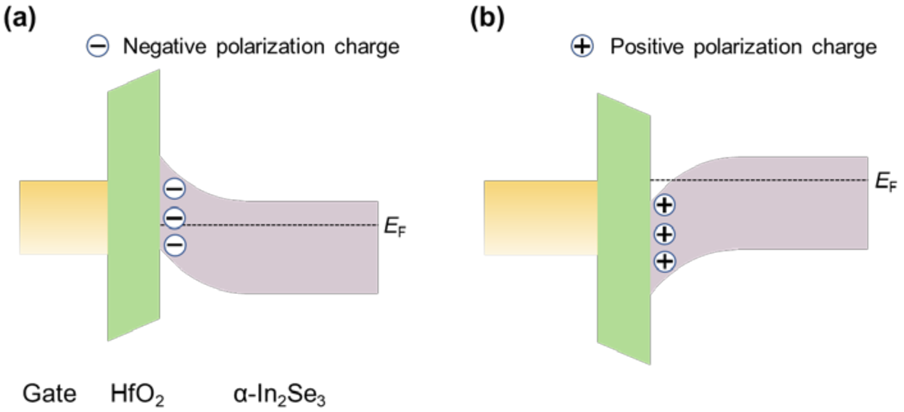

Supplementary Fig. S4 Band diagrams with the channel α-In_2Se_3 at different polarization states. **(a)** The band diagram after the device is set to the HRS due to a positive gate pulse applied ahead, in which negative polarization charges appear at the bottom surface of the channel α-In_2Se_3. **(b)** The band diagram after the device is stimulated to the LRS due to a negative gate pulse or a light pulse applied ahead, in which positive polarization charges appear at the bottom surface of the channel α-In_2Se_3 instead. Because a positive gate pulse can induce an upward electric field in channel α-In_2Se_3, an upward polarization is forced to appear and be strengthened so that negative polarization charges accumulate near the bottom surface of channel α-In_2Se_3 (a). For intrinsic α-In_2Se_3, the fermi level lies near the conduction band minimum, which endows it with n-type semiconducting nature. While in this HRS situation, the bounded negative polarization charges propel free electrons and induce an upward band bending near the surface, thus as a result, the fermi level shifts towards the valence band maximum near the surface, as shown in (a). On the contrary, a light pulse (or a negative gate pulse) induces the transition from upward polarization (HRS) to downward polarization (LRS) due to the downward imprint field, and then the resulting positive polarization charges near the bottom surface of the channel α-In_2Se_3 subsequently induces a downward band bending as shown in (b).

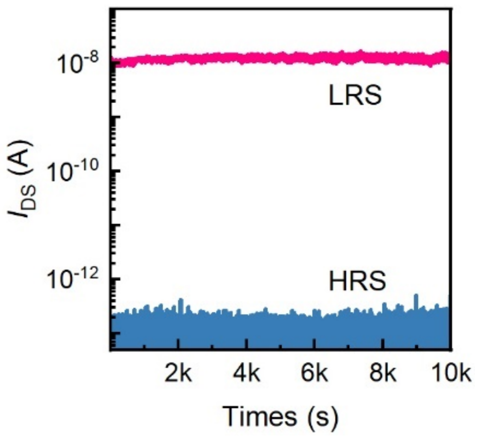

Supplementary Fig. S5 Long-term retention performance. The LRS was preset with a 360 nm light pulse of 4.4 fW and the HRS was preset with a gate pulse of 5 V.

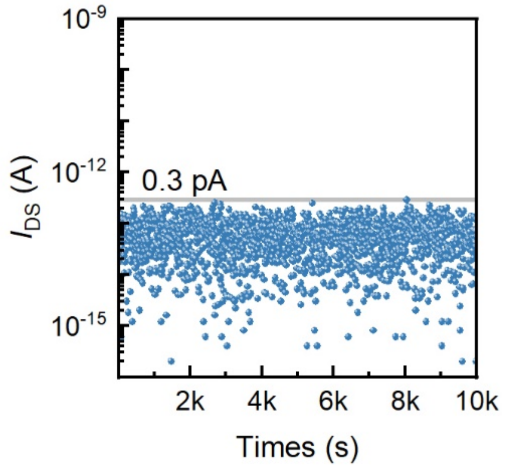

Supplementary Fig. S6 Retention of dark current (< 0.3 pA) for 10000 s. The device was preset to this low-current state with a positive gate pulse of 5 V amplitude. V_{read} = 1 V.

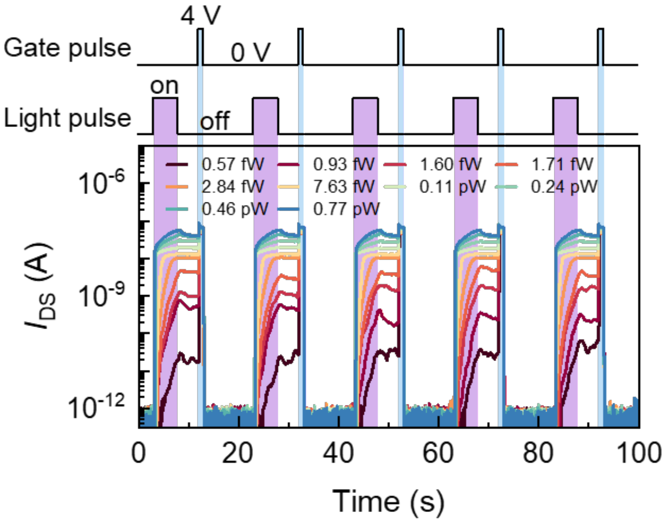

Supplementary Fig. S7 Temporal response to 360 nm light at various intensities. V_{DS}: 1 V.

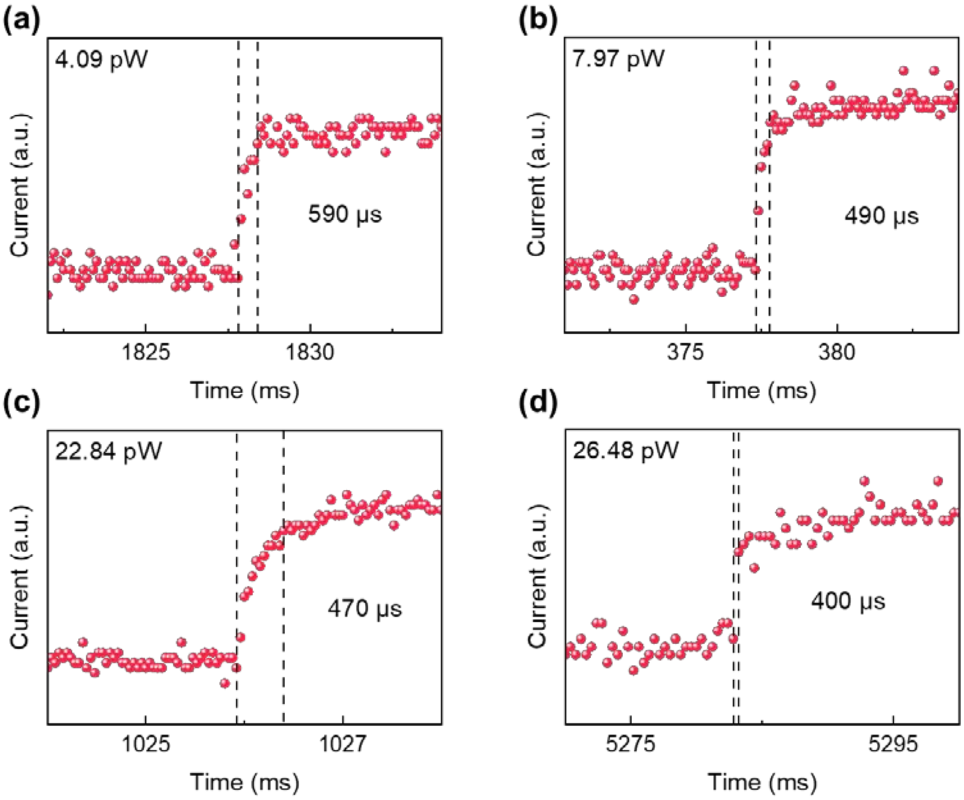

Supplementary Fig. S8 Response time of the device to 275 nm light at different intensities: **(a)** 590 µs at 4.09 pW, **(b)** 490 µs at 7.97 pW, **(c)** 470 µs at 22.84 pW, **(d)** 400 µs 26.48 pW.

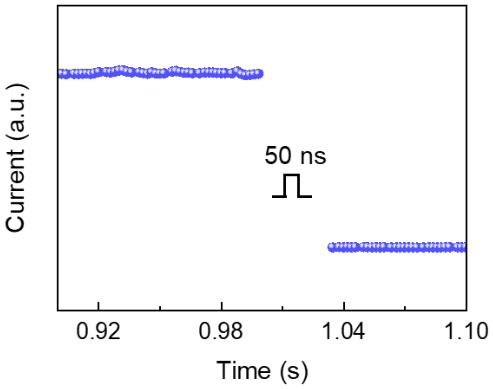

Supplementary Fig. S9 Response of the device to gate electrical pulse with a width of 50 ns.

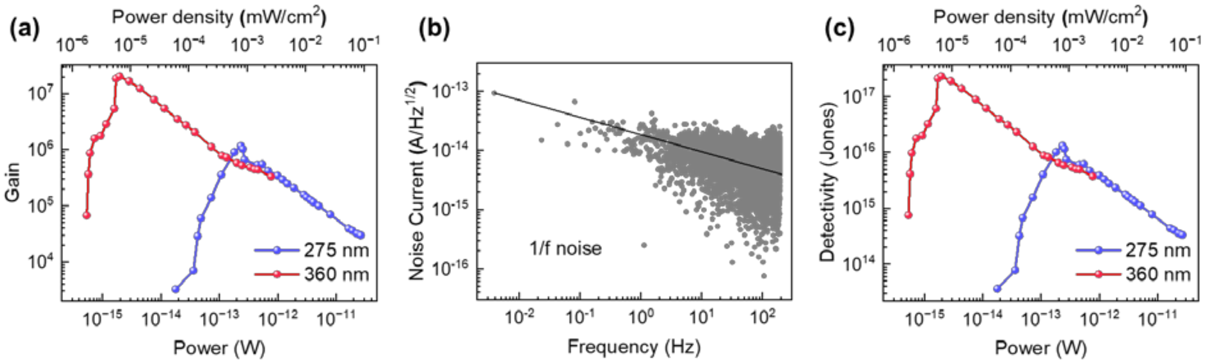

Supplementary Fig. S10 **(a)** Gain vs. power at 275 nm and 360 nm. **(b)** Noise current spectrum of the α-In$_2$Se$_3$ phototransistor. The dark line serves as a guide to the eye. **(c)** Detectivity vs. power at 275 nm and 360 nm.

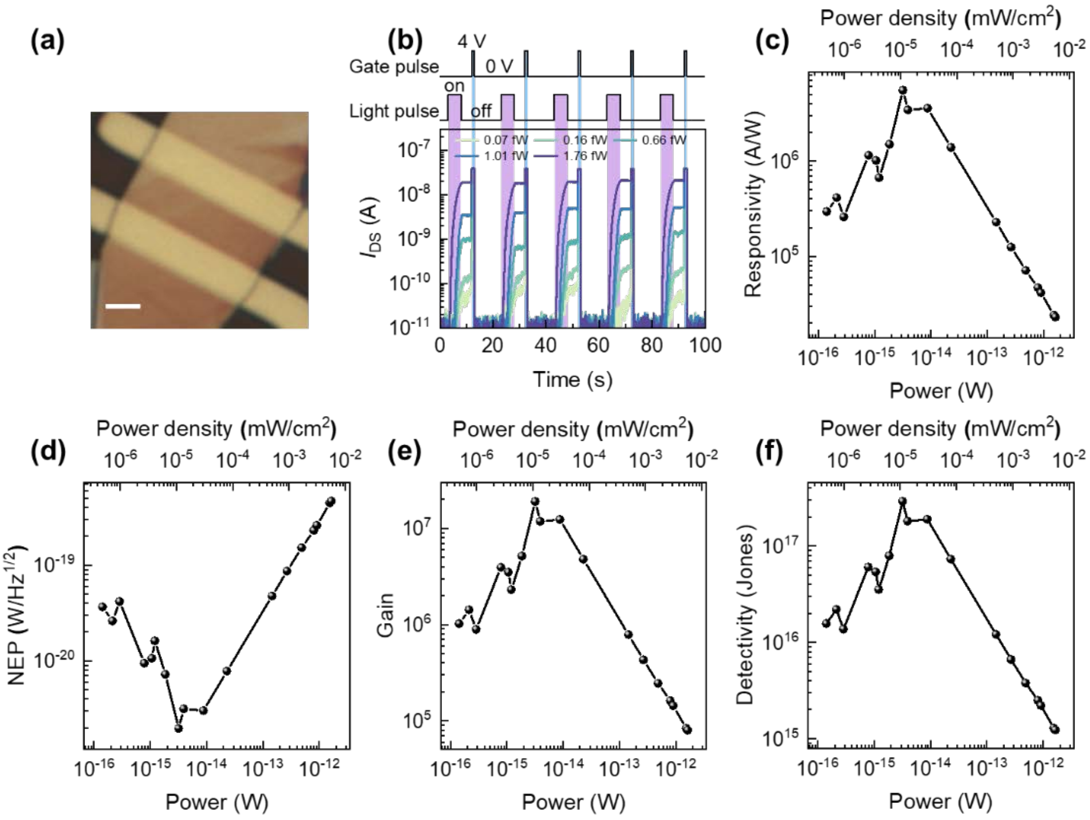

Supplementary Fig. S11 Another device's geometrical and optoelectronic performance. **(a)** OM image. Scale bar: 2 μm. **(b)** Temporal response to 5 cycles of alternating optical-electrical pulses, with light intensities ranging from 0.07 fW to 1.76 fW. V_{DS}: 1 V. Figures of merit vs. power: **(c)** responsivity, **(d)** NEP, **(e)** gain and **(f)** detectivity. Wavelength: 360 nm.

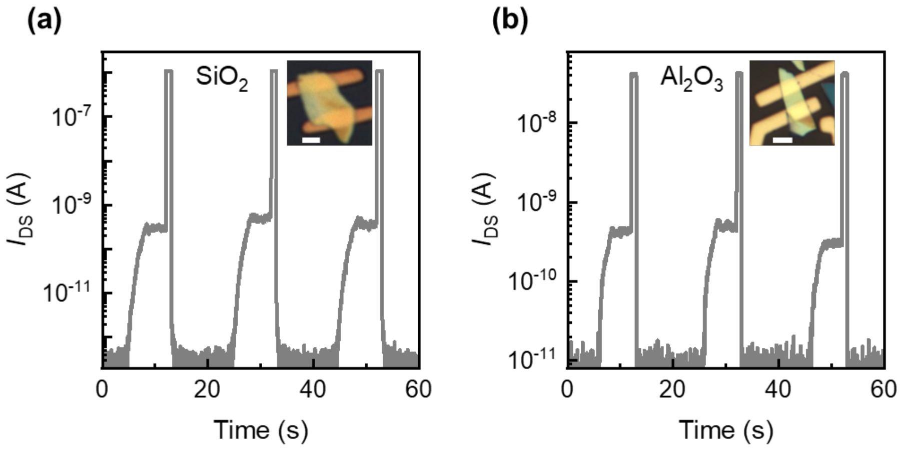

Supplementary Fig. S12 Temporal response curves of devices with **(a)** 90 nm-thick SiO_2 and **(b)** 50 nm-thick Al_2O_3 as dielectric layers. The insets are the optical microscope images of corresponding devices with scale bars of 2 μm. The temporal response curves were tested using 3 cycles of alternating optical and electrical pulses with a period of 20 s. Optical pulse: width 5 s, amplitude 14.14 fW (a) and 9.30 fW (b). Gate electrical pulse: width 1 s, amplitude 5 V (a) and 2 V (b). V_{DS}: 1 V.

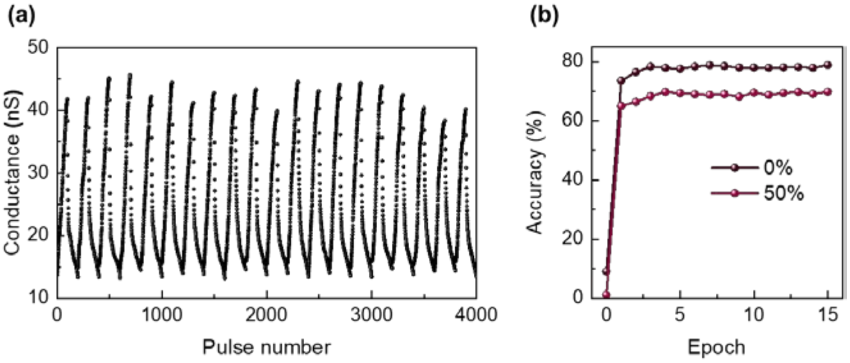

Supplementary Fig. S13 Demonstration of the α-In_2Se_3 phototransistor as a purely electrical synapse in an ANN. **(a)** Purely electrical pulse-dependent LTP and LTD behaviors of the synapse. During each conductance (weight) increasing/decreasing period, 100 negative/positive gate pulses with a width of 1 ms and an amplitude of -4/0.3 V were periodically applied with a period of 50 ms. **(b)** Recognition accuracy over F-MNIST dataset as a function of training epoch with different dataset noise levels: 0% and 50%.

Supplementary Table 1 Comparison of figures of merit among various materials/structures.

Material/structure	Power (W)	Responsivity (A/W)	Detectivity (Jones)	NEP (W/Hz$^{1/2}$)	Gain	Wavelength (nm)	Ref.
α-In_2Se_3	5.37×10^{-16}	4.5×10^{6}	2.3×10^{17}	2.4×10^{-21}	1.6×10^{7}	360	This work
α-In_2Se_3	1.79×10^{-14}	2.6×10^{5}	1.3×10^{16}	4.2×10^{-20}	1.2×10^{6}	275	This work
h-BN	3.25×10^{-12}	2.75	3.2×10^{13}	4.69×10^{-17}	21	160	[1]
$NiPS_3$	1.99×10^{-8}	0.126	1.22×10^{12}	2.32×10^{-16}	0.6	254	[2]
Graphene/β-Ga_2O_3	4×10^{-5}	39.3	5.92×10^{13}	1.51×10^{-14}	192	254	[3]
Te	8×10^{-11}	6.5×10^{4}	/	/	3.1×10^{5}	261	[4]
GaSe/WS_2	5×10^{-10}	3	/	/	11	350	[5]
BP/MoS_2	2.5×10^{-11}	207.3	/	/	920	280	[6]
BP	2.65×10^{-10}	9×10^{4}	3×10^{13}	1.21×10^{-17}	3.6×10^{5}	310	[7]
Graphene/h-BN/ZnO	1.25×10^{-6}	1.35×10^{4}	/	/	4.6×10^{3}	365	[8]
Bi_2Te_3	5.02×10^{-3}	6.3×10^{-3}	/	/	0.02	365	[9]
$SnS_2/ZnO_{1-x}S_x$	5.6×10^{-5}	8.28×10^{-3}	5.1×10^{10}	1.39×10^{-12}	0.03	365	[10]
$MnPS_3$	4.87×10^{-12}	288	6.48×10^{11}	8.79×10^{-16}	981	365	[11]
PbI_2	2×10^{-8}	0.51	4×10^{10}	1.12×10^{-13}	1.7	375	[12]
GaN	2.25×10^{-7}	2.5	/	4.5×10^{-13}	8.6	360	[13]
Diamond	2.4×10^{-4}	21.8	/	/	124	218	[14]
AlGaN	1×10^{-6}	200	/	/	765	325	[15]
Graphene QDs	4.2×10^{-6}	2.1×10^{-3}	9.59×10^{11}	3.3×10^{-13}	0.01	254	[16]
$MoS_2/Cs_3Bi_2I_9$	3.9×10^{-13}	1.42	1.15×10^{13}	1.45×10^{-16}	5.4	325	[17]
PEDOT:PSS/ZnO	1.38×10^{-4}	0.0035	7.5×10^{9}	3.27×10^{-11}	0.01	325	[18]
ZnO QDs/graphene	2.3×10^{-12}	9.9×10^{8}	1×10^{14}	1.3×10^{-18}	3.6×10^{9}	340	[19]
ZnO/Zn_2SnO_4	1.68×10^{-9}	3.5×10^{6}	9×10^{17}	5.56×10^{-20}	1.4×10^{7}	305	[20]

References

1. W. Zheng, R. Lin, Z. Zhang, and F. Huang, Vacuum-ultraviolet photodetection in few-layered h-BN, *ACS Appl. Mater. Interfaces* 10(32), 27116 (2018)
2. J. Chu, F. Wang, L. Yin, L. Lei, C. Yan, F. Wang, Y. Wen, Z. Wang, C. Jiang, L. Feng, J. Xiong, Y. Li, and J. He, High-performance ultraviolet photodetector based on a few-Layered 2D $NiPS_3$ Nanosheet, *Adv. Funct. Mater.* 27(32), 1701342 (2017)
3. W. Y. Kong, G. A. Wu, K. Y. Wang, T. F. Zhang, Y. F. Zou, D. D. Wang, and L. B. Luo, Graphene-β-Ga_2O_3 heterojunction for highly sensitive deep UV photodetector application, *Adv. Mater.* 28(48), 10725 (2016)
4. R. Cao, Y. Zhang, H. Wang, Y. Zeng, J. Zhao, L. Zhang, J. Li, F. Meng, Z. Shi, D. Fan, and Z. Guo, Solar-blind deep-ultraviolet photodetectors based on solution-synthesized quasi-2D Te nanosheets, *Nanophotonics* 9(8), 2459 (2020)
5. Q. Lv, F. Yan, X. Wei, and K. Wang, High-performance, self-driven photodetector based on graphene sandwiched GaSe/WS_2 heterojunction, *Adv. Opt. Mater.* 6(2), 1700490 (2018)
6. V. Krishnamurthi, M. X. Low, S. Kuriakose, S. Sriram, M. Bhaskaran, and S. Walia, Black phosphorus nanoflakes vertically stacked on MoS_2 nanoflakes as heterostructures for photodetection, *ACS Appl. Nano Mater.* 4(7), 6928 (2021)
7. J. Wu, G. K. W. Koon, D. Xiang, C. Han, C. T. Toh, E. S. Kulkarni, I. Verzhbitskiy, A. Carvalho, A. S. Rodin, S. P. Koenig, G. Eda, W. Chen, A. H. C. Neto, and B. Özyilmaz, Colossal ultraviolet photoresponsivity of few-layer black phosphorus, *ACS Nano* 9(8), 8070 (2015)
8. Z. Wu, X. Li, H. Zhong, S. Zhang, P. Wang, T. H. Kim, S. S. Kwak, C. Liu, H. Chen, S. W. Kim, and S. Lin, Graphene/h-BN/ZnO van der Waals tunneling heterostructure based ultraviolet photodetector, *Opt. Express* 23(15), 18864 (2015)
9. S. Yang, S. Jiao, H. Lu, S. Liu, Y. Nie, S. Gao, D. Wang, and J. Wang, Morphology evolution and enhanced broadband photoresponse behavior of two-dimensional Bi_2Te_3 nanosheets, *Nanotechnology* 32(43), 435707 (2021)
10. J. Jiang, J. Huang, Z. Ye, S. Ruan, and Y. J. Zeng, Self-powered and broadband photodetector based on $SnS_2/ZnO_{1-x}S_x$ heterojunction, *Adv. Mater. Interfaces* 7(20), 2000882 (2020)
11. R. Kumar, R. N. Jenjeti, M. P. Austeria, and S. Sampath, Bulk and few-layer $MnPS_3$: a new candidate for field effect transistors and UV photodetectors, *J. Mater. Chem. C* 7(2), 324 (2019)
12. H. Xiao, T. Liang, and M. Xu, Growth of ultraflat PbI_2 nanoflakes by solvent evaporation suppression for high-performance UV photodetectors, *Small* 15(33), 1901767 (2019)
13. T. Journot, V. Bouchiat, B. Gayral, J. Dijon, and B. Hyot, Self-Assembled UV photodetector made by direct epitaxial GaN growth on graphene, *ACS Appl. Mater. Interfaces* 10(22), 18857 (2018)
14. C.-N. Lin, Y.-J. Lu, X. Yang, Y.-Z. Tian, C.-J. Gao, J.-L. Sun, L. Dong, F. Zhong, W.-D. Hu, and C.-X. Shan, Diamond-based all-carbon photodetectors for solar-blind imaging, *Adv. Opt. Mater.* 6(15), 1800068 (2018)
15. E. Monroy, F. Calle, E. Muñoz, F. Omnès, B. Beaumont, and P. Gibart, Visible-blindness in photoconductive and photovoltaic AlGaN ultraviolet detectors, *J. Electron. Mater.* 28(3), 240 (1999)
16. Q. Zhang, J. Jie, S. Diao, Z. Shao, Q. Zhang, L. Wang, W. Deng, W. Hu, H. Xia, X. Yuan, and S.-T. Lee, Solution-processed graphene quantum dot deep-UV photodetectors, *ACS Nano* 9(2), 1561 (2015)

17. P. Zhang, Y. Zhang, W. Wang, L. Gao, G. Li, S. Zhang, J. Lu, Y. Yu, and J. Zhang, Multispectral photodetectors based on 2D material/$Cs_3Bi_2I_9$ heterostructures with high detectivity, *Nanotechnology* 32(41), 415202 (2021)

18. W. Peng, X. Wang, R. Yu, Y. Dai, H. Zou, A. C. Wang, Y. He, and Z. L. Wang, Enhanced performance of a self-powered organic/inorganic photodetector by pyro-phototronic and piezo-phototronic effects, *Adv. Mater.* 29(23), 1606698 (2017)

19. M. Gong, Q. Liu, B. Cook, B. Kattel, T. Wang, W. L. Chan, D. Ewing, M. Casper, A. Stramel, and J. Z. Wu, All-printable ZnO quantum dots/graphene van der Waals heterostructures for ultrasensitive detection of ultraviolet light, *ACS Nano* 11(4), 4114 (2017)

20. L. Li, L. Gu, Z. Lou, Z. Fan, and G. Shen, ZnO quantum dot decorated Zn_2SnO_4 nanowire heterojunction photodetectors with drastic performance enhancement and flexible ultraviolet image sensors, *ACS Nano* 11(4), 4067 (2017)